

# First Results from the AX-PET Demonstrator

P. Beltrame, E. Bolle, A. Braem, C. Casella, E. Chesi, N. Clinthorne, R. De Leo, G. Dissertori, L. Djambazov, V. Fanti, C. Joram, H. Kagan, W. Lustermann, F. Meddi, E. Nappi, F. Nessi-Tedaldi, J. F. Oliver, F. Pauss, M. Rafecas, D. Renker, A. Rudge, D. Schinzel, T. Schneider, J. Séguinot, P. Solevi, S. Stapnes and P. Weilhamer

**Abstract—** The AX-PET demonstrator is based on a new concept in PET detectors, with LYSO crystals aligned along the z coordinate (patient's axis) and WLS (Wave-length shifter) strips placed orthogonal to them. This kind of structure permits to avoid parallax errors due to different depths of interaction of the photons in the crystals, to register the three coordinates of the impinging photon and to reconstruct Compton events. In this way both the spatial resolution and the sensitivity can be highly improved. Moreover, as both the LYSO crystals and the strips are readout via Geiger-mode Avalanche Photo Diodes (G-APDs) the detector is insensitive to magnetic fields and is then suitable to be used in a combined PET/MRI apparatus. A complete Monte Carlo simulation and dedicated reconstruction software, suited to the particular geometry arrangement, have been developed. The two final modules, each composed by 48 crystals and 156 WLS strips have been built and fully characterized in a dedicated test set-up. The results on the performances of the system obtained with a  $^{22}\text{Na}$  point source (0.25 mm diameter) are reported.

## I. INTRODUCTION

A GOOD image quality in PET diagnostic exams is of outmost importance. One fundamental parameter is the detector spatial resolution, permitting the precise localization of tiny structures in brain PET and the tumor contour definition in oncology. Another important parameter is the detection efficiency whose increase could permit to reduce the dose to the patient or to enhance the image quality at the same dose level. The lowering of the dose could also open the path towards breast screening with PET or assure, in small animal imaging, a longer survival of the rodent. Nowadays poor spatial resolution and low efficiency limit the performances of the clinical scanners. The crystals used in present scanner geometries are arranged in rings in the radial direction with respect to the patient's axis. This arrangement limits in particular the spatial resolution and the sensitivity because of several reasons: The poor or absent knowledge of the depth of

interaction (DOI) smears the spatial resolution and makes it non-uniform in the whole field of view (FOV); smaller crystals that could improve DOI information also reduce the detection efficiency in the crystal; the poor rejection of Compton interactions due to their inefficient identification spoils the spatial resolution.

All the above considerations, together with the awareness that diagnostic needs are pushing towards multimodalities exams (e.g. PET/MRI), have led the AX-PET collaboration [1] to propose a completely different approach.

## II. THE AXIAL-PET CONCEPT

The Axial-PET concept is based on some basic assumptions. The scintillating crystals are aligned along the axis of the scanner (z axis). The layers of crystals are interleaved with layers of wave-length shifter strips (WLS), placed perpendicular to the crystals. A thin carbon foil is used to optically separate each plane composed by one layer of crystals and one layer of WLS. Both the crystals and the WLS are readout individually by Geiger-mode Avalanche Photo Diodes (G-APD) on one side, the other side being covered by a reflective coating (Fig.1).

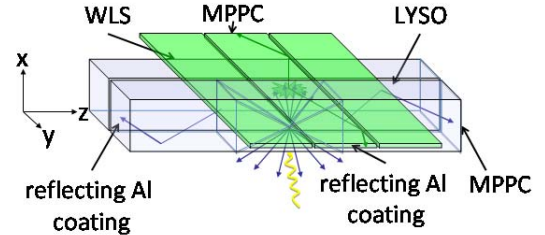


Fig.1. Two scintillating crystals (blue), placed parallel to the scanner axis, and three WLS strips (green), placed orthogonal to the crystals, are shown to depict the Axial-PET concept. One side of the crystals and the WLS is reflective, the other one being equipped with G-APD (MPPC). Following a gamma interaction, the light emitted by the crystal is in part detected by the MPPC and in part absorbed by the WLS, whose signals permit to reconstruct the z coordinate with high precision.

When a 511 keV photon interacts in one crystal, the light which is emitted inside the cone of total reflection travels along the crystal in both directions. The light emitted towards the photo detector and the light reflected by the opposite side is collected by the G-APD and provides the measurement of the energy of the impinging photon. The light escaping from the cone of total reflection in the crystal on the side where the WLS are placed can be absorbed (and re-emitted at a different wave length) by the WLS of the corresponding layer. As for the crystal, the light travels inside the strips in both directions

---

Manuscript received November 13, 2009.

P. Beltrame, A. Braem, V. Fanti, C. Joram, T. Schneider and J. Séguinot are with CERN, PH Department, CH-1211 Geneva, Switzerland.

C. Casella, G. Dissertori, L. Djambazov, W. Lustermann, F. Nessi-Tedaldi, F. Pauss, D. Schinzel, P. Solevi are with ETH Zurich, CH-8092 Zurich, Switzerland.

J. F. Oliver, M. Rafecas are with IFIC (UV-CSIC), E-46071 Valencia, Spain.

R. De Leo, E. Nappi are with INFN, Sezione di Bari, I-70122 Bari, Italy.

E. Chesi, H. Kagan, A. Rudge, P. Weilhamer are with Ohio State University, Columbus, Ohio 43210, USA.

D. Renker is with Paul Scherrer Institut, CH-5232 Villigen, Switzerland.

N. Clinthorne is with University of Michigan, Ann Arbor, MI 48109, USA.

E. Bolle, S. Stapnes are with University of Oslo, NO-0317 Oslo, Norway.

F. Meddi is with University of Rome "Sapienza", I-00185 Rome, Italy.

V. Fanti is on leave of absence from Università e Sezione INFN di Cagliari, Italy (corresponding author, e-mail: viviana.fanti@cern.ch).

through total internal reflection, is reflected on one side and is collected at the other side by the photo detector.

The DOI information ( $x$  and  $y$  coordinates) is given by the knowledge of the crystal that has been hit. The spread on the  $x$  and  $y$  coordinates is given by  $\sigma_{x,y} = d / \sqrt{12}$ ,  $d$  being the crystal width. The  $z$  coordinate of the point of interaction can be determined by the signal of the WLS. The light is usually absorbed by more than one WLS so that a weighted average can be used to extract the  $z$  coordinate. In this way the spatial resolution can be improved with respect to the digital resolution ( $\sigma = d / \sqrt{12}$ , with  $d$  equal to the width of the strip).

In previous measurements [2]-[5] it has been demonstrated that the light yield from WLS strips is sufficiently high to allow observation in the WLS strips of the 511 keV photo absorption events in the crystals. The Compton interactions can also be registered in the WLS, provided that the energy of the recoil electron is at least 100 keV. Energy deposition from Compton interactions below 100 keV can still be observed in the LYSO crystal matrix but without measurements of the axial coordinate. These interactions can be removed from the event sample before the image reconstruction.

#### A. Expected advantages of the Axial-PET concept

The Axial-PET concept allows the 3D reconstruction of the impact point of the impinging photon both for photoelectric and for Compton interactions. The parallax error due to lack of information on DOI – inherent to radial geometries – can thus be overcome.

The detection efficiency depends on the total crystal thickness and can be simply increased using a larger number of crystal layers. Moreover, the possibility of including in the image reconstruction part of the Compton events, leads to an increase in sensitivity.

The spatial resolution depends on the transverse size of the crystals and of the WLS and can be tuned depending on the foreseen application.

As a last point, using G-APD as photo detectors makes the device insensitive to magnetic fields and suitable for the construction of a combined PET/MRI apparatus.

In order to prove all the above mentioned advantages, we have built a demonstrator composed by two modules.

### III. THE AX-PET DEMONSTRATOR

The AX-PET demonstrator is composed by two identical modules. Each module has 48 crystals and 156 WLS arranged in a stack of six layers (Fig. 2). Each layer, with eight crystals and 26 WLS, is optically separated from the next one by a thin carbon fiber plate. The crystals in even layers are staggered with respect to the crystals in odd layers by half the pitch size, so that the spaces between the crystals do not line up.

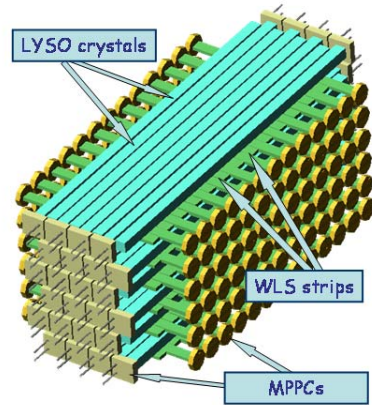


Fig.2. Drawing of one of the two modules of the AX-PET demonstrator. Six layers of eight crystals each are interleaved with six layers of WLS. The MPPCs are mounted alternately on one side or the other of the module in order to avoid dead areas. Each double layer composed by crystals and strips is optically isolated from the next one by a thin carbon fiber plate (not shown). The crystals in adjacent layers are staggered by half a pitch size.

#### A. Description of the components

The scintillating crystals are LYSO type from Saint-Gobain (PreLudeTM 420), with chemical formula  $\text{Lu}_{1.8}\text{Y}_2\text{SiO}_5:\text{Ce}$ . The LYSO is a non-hygroscopic material, has density of 7.1 g/cm<sup>3</sup>, light yield 32 photons/keV, attenuation length (at 511 keV) 1.2 cm, scintillation decay time 42 ns, single exponential. LYSO naturally contains a certain amount of the isotope <sup>176</sup>Lu, which decays by  $\beta$  emission followed by prompt emission of three gamma rays. As explained later, two of these gammas are used for the energy calibration of the modules.

Each LYSO crystal has dimensions 3 mm × 3 mm × 100 mm and has been characterized in a dedicated set-up [6].

The WLS strips, from Eljen Technology (type EJ-280 with a dye concentration ten times higher than standard material), have dimensions 0.9 mm × 3 mm × 40 mm and are placed orthogonally to the crystals. Their maximum peak in the absorption curve correctly matches the peak emission wave length of the LYSO (425 nm). The WLS have also been characterized in a dedicated set-up [5].

Both the LYSO crystals and the WLS are readout on one side by fast photo detectors (G-APD) from Hamamatsu (MPPC: Multi Pixel Photon Counter) glued with an optical glue, the other side being covered with an Al coating to make it reflective. The MPPCs used for the crystals are of standard type (S10362-33-050C, 3600 cells 50 μm × 50 μm, dimension 3 mm × 3 mm), while for the WLS they are custom made by Hamamatsu (OCTAGON-SMD, 782 cells 70 μm × 70 μm, dimension 3.22 mm × 1.19 mm). Most of the MPPC have been characterized individually in a dedicated set-up [5].

Fig. 3 shows the pictures of different components during the mechanical assembly, one of the crystals glued to the MPPC and several WLS strips glued to the MPPCs, in turn soldered to the kapton flex prints. Fig. 4 shows one of the two modules after being fully assembled.

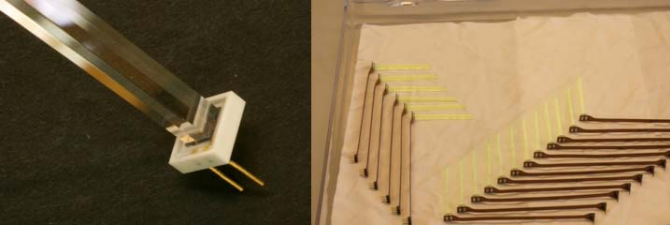


Fig.3. The photo on the left shows one LYSO crystal glued to one MPPC. The photo on the right shows several WLS strips (green) glued to the MPPC, in turn soldered to the kapton flex prints.

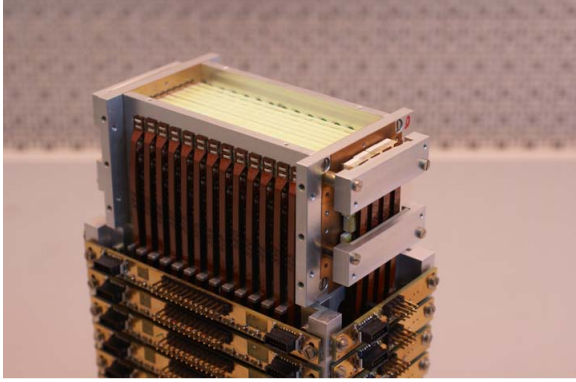


Fig.4. One of the two modules at the end of the mechanical assembly. The kapton flex prints are clearly visible together with the patch panels housing the connectors for the MPPCs bias voltage and for the output signals.

In the two modules the MPPCs are mounted alternately on one side and on the opposite one, so that the system can be made as compact as possible. The pitch is 3.5 mm in a crystal plane and 3.2 mm in a WLS plane. The distance between two layers in the direction of the impinging photons is 7 mm.

### B. Readout electronics

The signals out of the MPPCs are distributed to a patch panel via kapton strip line cables about 15 cm long. From the patch panel the MPPC signals are transmitted via thin coaxial cables to a master PCB equipped with fast amplifiers (OPA846). The output of each one of the fast amplifiers is threefold: (i) a direct short connection (line on PCB) via a 100 k $\Omega$  resistor, turning the voltage signal into a high impedance current signal, to the input of the VATAGP5 chip [7] which is mounted on a separate PCB joined via a connector to the master PCB; (ii) in parallel the signals from the LYSO crystals are routed to a circuitry allowing to add signals from groups of channels or all channels to build a pulse height sum which is used in the external trigger to select 511 keV events; (iii) the signals of each channel are also available on a parallel twisted output via a line driver for test purposes.

The VATAGP5 chip has a sparse readout option. Only channels with a signal above a chosen threshold in the fast branch of the chip will be stored in the readout register for this channel and the corresponding slow shaper amplitude of only these channels will be readout subsequently. The self-triggering feature of the readout is used for specific tests and calibrations, while for the demonstrator set-up data taking an external trigger is used (see below).

### C. Temperature and MPPC gain control

The modules are kept in an air-conditioned dark room but are not individually cooled. The temperature is constantly monitored by means of four sensors (AD590) placed on the module frame, and recorded by a LabVIEW program. This is necessary since the gain of a MPPC is strongly temperature dependent. The knowledge of the temperature permits to change the supply voltage of the MPPC in order to maintain a constant gain. If the temperature changes during data taking, gain corrections can be applied in the offline analysis. The bias voltages for all the 408 MPPCs of the two modules can be individually set and are controlled by a custom built control box using 32 channel voltage DACs controlled by a LabVIEW program.

## IV. EXPERIMENTAL SET-UP FOR THE CHARACTERIZATION OF THE MODULES

The two modules have been individually calibrated in a test set-up, shown in Fig. 5, using a point-like  $^{22}\text{Na}$  source (activity 925 kBq, diameter 250  $\mu\text{m}$ ). Two tagging LYSO crystals, readout with a fast PMT, are used for energy calibration and studies of axial spatial resolution. One of them has dimensions 2 mm  $\times$  10 mm  $\times$  12 mm and is used for the uniform illumination of the crystals. The other one has dimensions 2 mm  $\times$  2 mm  $\times$  12 mm and allows the definition of a beam spot size of about 1 mm on the closest layer of crystals (Fig. 6). The tagging crystal and the source holder are mounted on a computer controlled translation table, which allows precise positioning of the source image on the PET module in two directions (y and z).

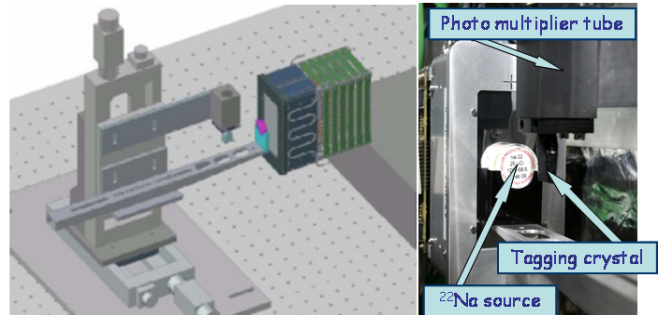


Fig.5. Set-up for the characterization of the modules. On the left a drawing of one module and the mechanical assembly is shown. The  $^{22}\text{Na}$  source and the tagging crystal are mounted on a 2D translation table remotely controlled.

### A. The trigger

The trigger used for these tests consists of a coincidence of the sum of all 48 LYSO signals from one module with a signal from one of the tagging crystals. In this way, the annihilation events with one gamma interacting in the module and one gamma interacting in the tagging crystal are selected. The signals in the WLS strips are not used in the trigger. During data taking the *Data Lock* (DL) option of the readout chip is switched on. Thus during the waiting time for a trigger, hits with signals above the internal threshold of the front-end chip will not be validated in the chip output register. Once a trigger

is produced, the output of the coincidence unit pulls the DL line on the chip low for about 100 ns. During this time, all hits occurring in the whole module will be written into the output register of the chip for subsequent readout.

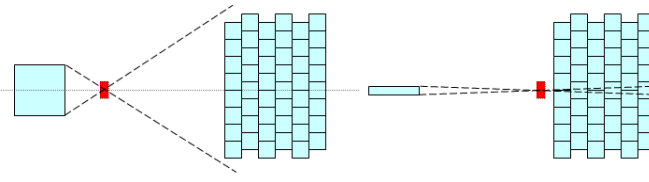


Fig. 6. On the left: the beam spot selected by using the big tagging crystal in the coincidence trigger is shown (seen from the top). The uniform illumination of the crystals is used for the energy calibration.. On the right the small beam spot as obtained using the small tagging crystal in the trigger is shown. The precise definition of the position of the beam spot permits to study the spatial resolution of the module.

### B. The data acquisition

The data acquisition system makes use of custom made VMEbus boards based on XILINX fPGA. One VME board controls one module and receives the signals from the intermediate board which synchronizes the signals of the four VATAGP5 chips used for one module.

The data acquisition software communicates with the slow control PC at the beginning of each run of data taking through the DIM protocol [8]. The communication is used to read the temperature of the module and store it in the data file and, if required, instruct the motion control program to step to the next y-z position and store the new coordinates in the data file.

## V. RESULTS FROM THE CALIBRATION OF THE MODULES

The experimental set-up just described has been used to characterize individually the two modules. Data have been taken with the internal trigger (VATAGP5 self-triggering mode) to acquire intrinsic radioactivity spectra from  $^{176}\text{Lu}$  to be used for energy calibration, and with the external trigger described in previous sections to acquire data with the  $^{22}\text{Na}$  source.

### A. Module occupancy

In Fig. 7 a box plot shows the occupancy of one of the two modules when the module is uniformly illuminated by the source and when the image of the source is a small spot as defined by the coincidence with the small tagging crystal (see Fig. 6). It can be observed that in the first case the response of the crystals in one layer is uniform. The attenuation of the beam in depth is also clearly seen.

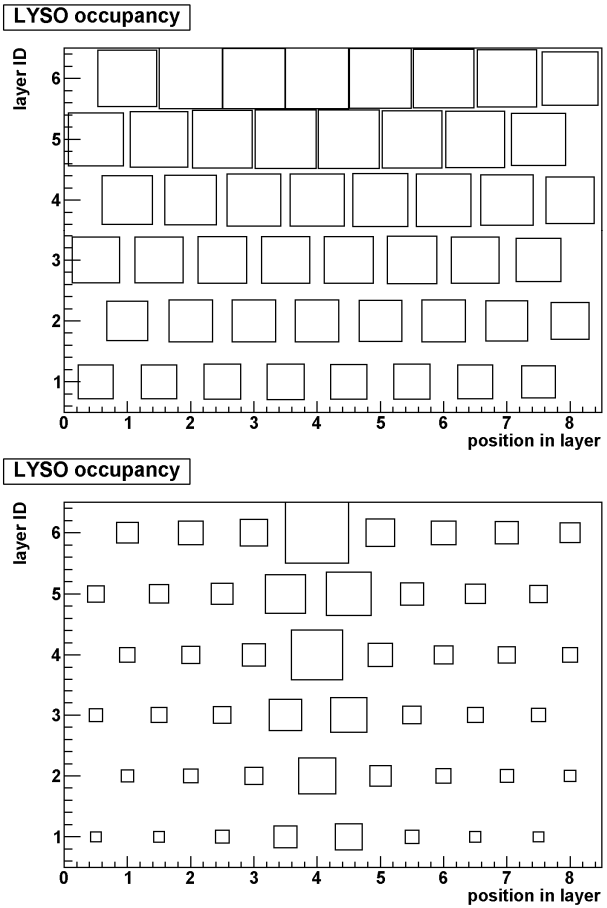


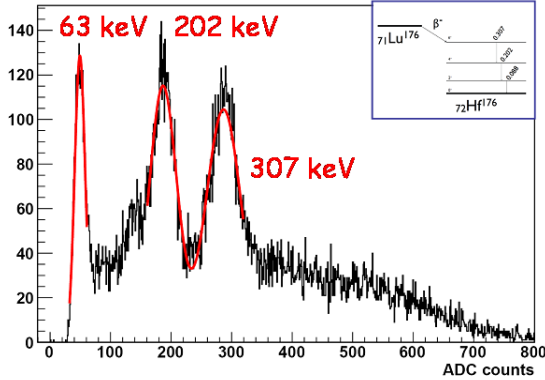
Fig. 7. Occupancy in one of the modules. The size of each box is proportional to the number of hits in the crystal. On the top the trigger is formed using the coincidence between the module and the big tagging crystal, on the bottom the small tagging crystal is used. Layer no. 6 is the first one that is seen by the beam. The staggering of the crystals is also shown.

### B. Energy calibration

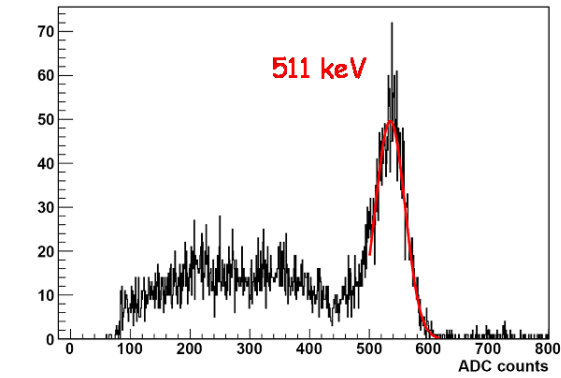
In order to determine the energy calibration curve we use two different data sets. The first one (acquired in self-triggering mode), comprises two of the peaks of the  $^{176}\text{Lu}$  decay spectrum at 202 and 307 keV and the Lutetium K<sub>a</sub> escape line at 63 keV. The second one (acquired with the  $^{22}\text{Na}$  source and the big tagging crystal) comprises the photoelectric peak at 511 keV. The four peaks are fitted with a Gaussian function.

A negative logarithmic function is used to fit the four data points to take into account the saturation effect in the MPPCs occurring at the photoelectric peak energy. An example of the energy calibration in one of the LYSO crystals is shown in Fig. 8. All the 48 crystals of each module are calibrated in the same way.

LYSO No. 21 - intrinsic radioactivity



LYSO No. 21 - 22Na coinc. trigger



Calibration: En\_vs\_ADC - LYSO21

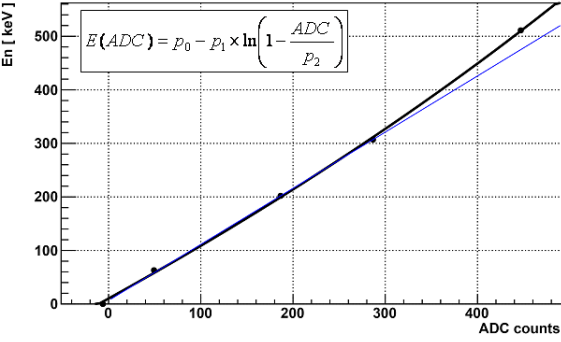


Fig. 8. Top: the spectrum measured by one LYSO crystal showing the two peaks of the intrinsic radioactivity of  $^{176}\text{Lu}$  at 202 and 307 keV and the Lu K $\alpha$  escape line at 63 keV (data acquired in self-triggering mode and low discriminator threshold). Middle: the spectrum measured by the same crystal when the  $^{22}\text{Na}$  source is in place and the coincidence trigger with the big tagging crystal is used. Gaussian fits are used to extract the values of the ADC counts corresponding to the four peaks. In the bottom plot these values are shown together with the negative logarithmic function used to fit the data (black line). The deviation from linearity (blue line) arises from the saturation in the MPPC (~5% effect).

### C. Energy resolution

After applying the energy calibration, the energy resolution of the module can be derived. The results obtained for single LYSO crystals and for the sum (event per event) of the energies of all the crystals of one module (Fig. 9), show an energy resolution  $\Delta E/E = 11.7\%$  FWHM (at 511 keV) as average of the single crystals and 12.5% FWHM (at 511 keV)

in the sum. The spectrum of the crystals is well fitted by a double Gaussian, the second peak due to the missing energy of the Lu K $\alpha$  escape line (63 keV). Comparable values of energy resolution are found for the other module.

Energy resolution

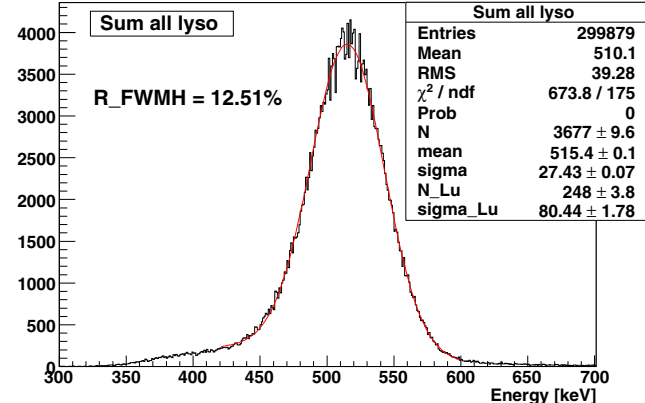
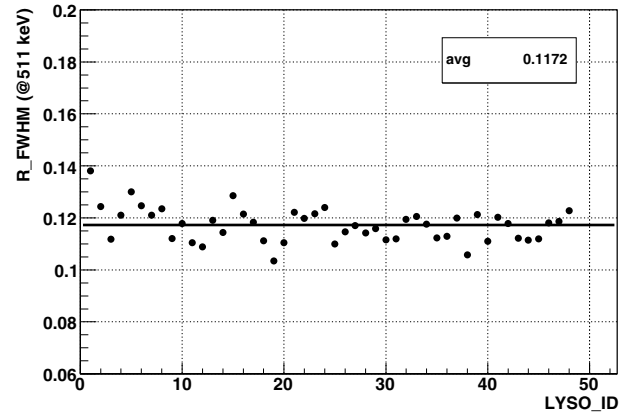


Fig. 9. Top:  $\Delta E/E$  (FWHM) at 511 keV for each single crystal of one of the modules. The mean value is 11.7%. Bottom: energy distribution of the sum of all the crystals of one module. The relative width of this distribution is  $\Delta E/E = 12.5\%$  FWHM at 511 keV. The results for the other module (not shown) are very similar.

### D. Spatial resolution

The data taken with the collimated spot size permit to determine the axial (z) coordinate using the signals from the WLS strips. Events with just one cluster of WLS strips corresponding to a single LYSO crystal hit in the matrix are selected (photoelectric events). The distributions of the WLS strip position, weighted with the corresponding signal amplitudes (center of gravity method) are plotted for each layer of one module in Fig. 10. A Gaussian fit on these distributions provides the z coordinate (mean) and an estimate of the spatial resolution in the axial direction  $\sigma_{\text{meas}}$ . This value differs from the intrinsic spatial resolution  $\sigma_{\text{intr}}$ , as it includes the contribution of the beam spot size  $\sigma_{\text{beam}}$  which increases with the distance of the layer from the source:

$$\sigma_{\text{meas}} = \sqrt{\sigma_{\text{intr}}^2 + \sigma_{\text{beam}}^2}$$

In order to extract the correct value of the intrinsic spatial resolution, the diameter of the spot is supposed to vary linearly with the distance  $d$  from the source, being negligible at  $d=0$  (this assumption can be made as the source diameter is only 250  $\mu\text{m}$ ). Fig. 11 plots the square of  $\sigma_{\text{meas}}$  as a function of the square of the distance. The intercept of the straight line which fits the data at  $d=0$  gives the squared value of the intrinsic spatial resolution. It is then obtained  $\sigma_{\text{intr}} = 0.58 \text{ mm}$  corresponding to 1.4 mm FWHM. This is a preliminary value corresponding to a particular selection of data (photoelectric events) for module 1. The analysis of the data relative to all events and both modules is ongoing.

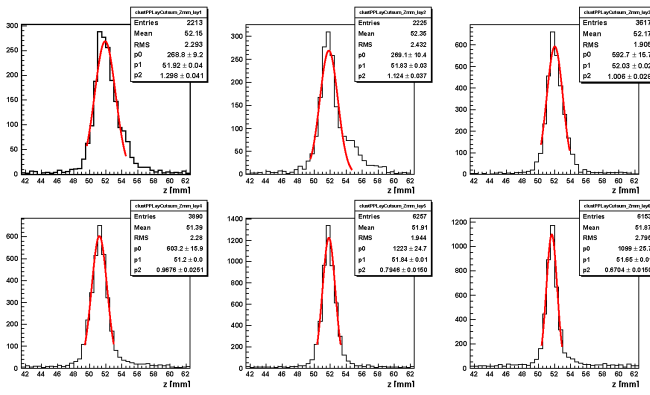


Fig. 10. Distributions of the reconstructed  $z$  coordinate in each of the six layers of module 1 for photoelectric events. Superimposed is shown the Gaussian fit from which the measured spatial resolution  $\sigma_{\text{meas}}$  is derived. Layer 2 shows a tail at high  $z$  values due to a noisy WLS strip channel.

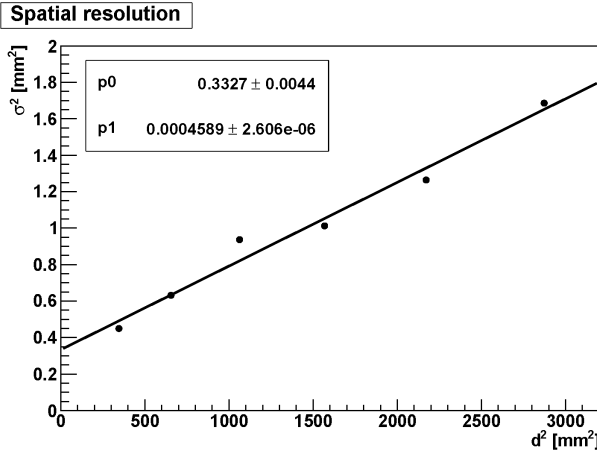


Fig. 11. Square of the measured spatial resolution for each of the six layers as a function of the square of the distance of the layer from the source. The interpolation at zero distance ( $p_1$ ) gives the squared value of the intrinsic spatial resolution.

### E. Simulation and image reconstruction

In order to estimate the performance of the entire system, the AX-PET demonstrator has been fully simulated using GEANT4 and GATE packages. For the image reconstruction the Maximum-Likelihood Expectation Maximization (MLEM) algorithm has been implemented. To increase the sensitivity of

the device, inter-crystal scatter events are identified and reconstructed with an efficiency of at least 70%.

For two opposite rotating modules, simple phantoms (cylinder, sphere and point sources) have been simulated and reconstructed with MLEM. System Matrix has been computed using Siddon's ray-tracing algorithm. An example is shown in Fig. 12.

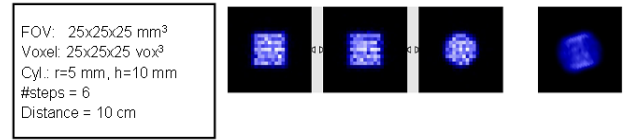


Fig. 12. Reconstruction of a uniform cylinder source simulated in realistic run conditions.

## VI. CONCLUSIONS

The two modules of the AX-PET demonstrator have been built and fully characterized. Preliminary results are very encouraging. An energy resolution of 12.5% FWHM at 511 keV on the sum of all crystals of one module and 11.7% FWHM at 511 keV as average of the single crystals has been measured. The spatial resolution in the axial direction is found to be 1.4 mm FWHM for photoelectric events.

The next steps will be the measurements in coincidence between the two modules, first with point sources then with PET phantoms filled with  $^{18}\text{F}$  radiotracer mounted on a rotating gantry. These last tests will take place at ETH Zurich, Institute for Radiopharmaceutical science, starting at the beginning of 2010. The mechanical structure for the tests has been already built and assembled.

## REFERENCES

- [1] <https://twiki.cern.ch/twiki/bin/view/AXIALPET/WebHome>
- [2] J. Séguinot et al., "Novel Geometrical Concept of a High Performance Brain PET Scanner- Principle, Design and Performance", Il Nuovo Cimento C, Volume 29 Issue 04 (2005) p 429
- [3] A. Braem et al., "Scintillator Studies for the HPD-PET Concept", Nucl. Instr. Meth. A 571 (2007) 419-424.
- [4] A. Braem et al., "High precision Axial Coordinate Readout for an Axial 3-D PET Detector Module using a Wave Length Shifter Strip Matrix", Nucl. Instr. Meth. A 580 (2007) 1513-1521.
- [5] A. Braem et al., "Wave Length Shifter Strips and G-APD Arrays for the Read-Out of the  $z$ -Coordinate in Axial PET Modules", Nucl. Instr. Meth. A 586, (2008) 300-308.
- [6] E. Bolle et al., "Development of a High Precision Axial 3-D PET for Brain Imaging", presented at 11th Topical Seminar on Innovative Particle and Radiation Detectors (IPRD08) 1 - 4 October 2008 Siena, Italy, submitted for publication to Proceedings. Nucl.Phys. B, Proc. Suppl.
- [7] E. Chesi et al., "A segmented hybrid photon detector with integrated auto-triggering front-end electronics for a PET scanner", Nucl. Instr. Meth. A 564 (2006) 352-363.
- [8] C.Gaspar, M. Dönszelmann, Ph.Charpentier, "DIM, a Portable, Light Weight Package for Information Publishing, Data Transfer and Inter-process Communication", Presented at: International Conference on Computing in High Energy and Nuclear Physics (Padova, Italy, 1-11 February 2000).